

Win X-ray: A New Monte Carlo Program that Computes X-ray Spectra Obtained with a Scanning Electron Microscope

Raynald Gauvin,^{1,*} Eric Lifshin,² Hendrix Demers,¹ Paula Horny,¹ and Helen Campbell¹

¹Department of Metals and Materials Engineering, McGill University, Montréal, Québec H3A 2B2, Canada

²College of Nanoscale Science and Engineering, University at Albany, CESTM, 251 Fuller Road, Albany, NY 12203, USA

Abstract: A new Monte Carlo program, *Win X-ray*, is presented that predicts X-ray spectra measured with an energy dispersive spectrometer (EDS) attached to a scanning electron microscope (SEM) operating between 10 and 40 keV. All the underlying equations of the Monte Carlo simulation model are included. By simulating X-ray spectra, it is possible to establish the optimum conditions to perform a specific analysis as well as establish detection limits or explore possible peak overlaps. Examples of simulations are also presented to demonstrate the utility of this new program. Although this article concentrates on the simulation of spectra obtained from what are considered conventional thick samples routinely explored by conventional microanalysis techniques, its real power will be in future refinements to address the analysis of sample classifications that include rough surfaces, fine structures, thin films, and inclined surfaces because many of these can be best characterized by Monte Carlo methods. The first step, however, is to develop, refine, and validate a viable Monte Carlo program for simulating spectra from conventional samples.

Key words: X-ray microanalysis, Monte Carlo, scanning electron microscopy, energy dispersive spectrometry, electron scattering

INTRODUCTION

A new program is described that predicts full X-ray spectra measured with an energy dispersive spectrometer (EDS) attached to a scanning electron microscope (SEM). It is based on the simulation of electron scattering in solids using the Monte Carlo method described by Gauvin and L'Espérance (1992) for X-ray microanalysis in the transmission electron microscope and by Hovington et al. (1997) for X-ray microanalysis in the SEM; these methods are an extension of previous work by Bishop (1965) and by Karduck and Rehbach (1991).

Previous attempts that have been made to compute complete X-ray spectra generally fall into two categories, closed form analytical models and Monte Carlo models. Because of uncertainties in either the correctness of the physical models or the parameters used in both approaches, they must be refined with the use of some adjustable parameters to achieve a close match with experimental spectra. Examples of the analytical model approach include the Desktop Spectrum Analyzer (DTSA) described by Fiori and Swyt (1989) and more recently an approach described by Dun-

cumb et al. (2001). The former is readily available from the National Institute for Standards and Technology (NIST) at no charge; however its operation is limited to Apple computers. The general availability of the latter program is not known at this time although many of the equations used in its development are described in the reference. This reference also specifies that the RMS error between measured and simulated peak intensities was determined to be 7.1% for 360 *K*, *L*, and *M* peaks from known standards. Very good agreement was also found for peak to integrated total background ratios. This approach is therefore very promising for estimating spectra for thick samples and standards for conventional electron microprobe analysis where the electron excitation volume and absorption paths are well contained in the region being analyzed. The second approach, that of Monte Carlo modeling, has been described by Ding et al. (1994), who computed the bremsstrahlung using Monte Carlo simulations; however, their work was limited to pure elements and normal electron beam incidences and furthermore absolute X rays were not computed.

More recently the Monte Carlo program PENELOPE has been applied to the generation of complete X-ray spectra, including characteristic and continuum peaks; however, its initial use was limited to *K* lines and *L* lines by Llovet et al. (2004). The results are given in photon/electron/steradian as a function of energy and a very large number of

trajectories are required to compute a full spectrum, thus taking many hours of computer time. Because the Monte Carlo approach even with some simplification is inherently more time consuming than closed form modeling, it is not unreasonable to ask "Why bother using it?" if the accuracy and computation time of closed form modeling is considerably better. The answer is that, for conventional analysis, it may not be particularly useful beyond predicting absolute X-ray spectra and detectability limits. However, many practical samples examined cannot be described easily or even at all by modifications of conventional models, and Monte Carlo modeling may be the only viable approach. Furthermore Monte Carlo calculations may facilitate a more conventional closed form approach. An example of the latter might be the generation of a calibration curve of K ratio versus film thickness. Examples of nonconventional analysis include rough surfaces, fine structures, thin films, and inclined surfaces.

Before Monte Carlo methods can truly be shown to be accurate in addressing the more complex analytical cases listed, it was felt that a program should first be developed that accurately predicts the complete spectra expected from conventional samples using normal electron beam incidence to the specimen surface. It was further felt that a new program should be relatively easy to use, fast, generally available, as is DTSA, and that all of the details of the underlying model be fully disclosed. What is described here is such a program, *Win X-ray*, designed to simulate the total X-ray spectra (the characteristic lines and the bremsstrahlung) for homogeneous alloys or compounds at any angle of the incident electron beam and the X-ray detector takeoff angle. Furthermore, this program computes absolute X-ray intensities in order to simulate real experimental conditions for incident electron energies ranging from 10 to 40 keV. Results can then be used for a variety of applications, including the calculation of detection limits, peak-to-background ratios, performance optimization, and comparison with experimental results to aid in both qualitative and quantitative analysis. *Win X-ray* can be downloaded at <http://www.montecarlomodeling.mcgill.ca/>. It should be viewed as a first step in the development of a more accurate and versatile Monte Carlo model to handle nonconventional samples.

DESCRIPTION OF THE MONTE CARLO PROGRAM

A general description of how Monte Carlo calculations are used to predict electron solid interactions can be found in a number of references including Joy (1995) and Gauvin et al. (1995). The process involves calculating the trajectories of a large number of electrons striking a sample one at a time. Although the same general equations are used to calculate the position and energy of each electron along its trajectory,

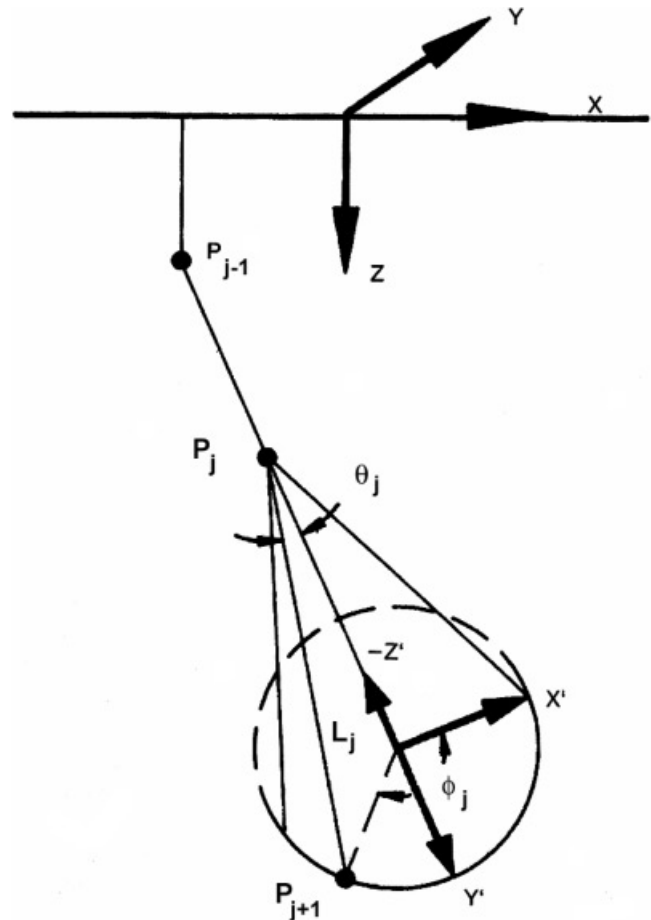


Figure 1. Geometry used to simulate the trajectories of electrons using a single scattering approach. When an electron suffers a collision at a point P_j , the trajectory is changed by polar and azimuth angles, θ_j and ϕ_j , respectively. Also, this electron travels a distance L_j to the point P_{j+1} , where it suffers another collision.

the details vary for each electron trajectory because of the use of random numbers to simulate the actual variability of the process. Figure 1 shows the geometry used to simulate the trajectories of electrons using a single scattering approach. When an electron suffers a collision at a point P_j , the trajectory is changed by polar and azimuth angles θ_j and ϕ_j , respectively. Also, this electron travels a distance L_j to the point P_{j+1} , where it suffers another collision. From P_j to P_{j+1} , the electron loses energy, and it is evaluated using the continuous slowing down approximation. Between each collision, the generated X rays are computed. In *Win X-ray*, the effects of fluorescence on X-ray generation are not as yet included, although they will be added in later versions of the program. The electron trajectory is stopped when the energy is lower than the smallest continuous energy computed or when it escapes the specimen as a backscattered electron.

Win X-ray was written using the C++ language under Borland C++ Builder to develop the Windows™ interface.

The language structure was developed to insert separate blocks allowing different types of specimen geometry to be simulated. In this article, we report the simple case of a bulk homogeneous and flat material. New versions with various types of specimen geometry are currently under development.

Total Elastic Cross Sections

In *Win X-ray*, either Mott or Rutherford total elastic cross sections are used. Mott cross sections are recommended because they are more accurate for electron energy below 30 keV because, unlike Rutherford cross sections, they are not based on the first Born approximation. The superiority of Mott over Rutherford cross sections in Monte Carlo simulations for energies below 30 keV was shown by Drouin et al. (1997). The tabulated values of the total Mott cross sections computed by Czyzewski et al. (1990) are used in *Win X-ray*.

For energies above 30 keV, the first Born approximation is appropriate and the Rutherford elastic cross sections are used. The equation to compute the total Rutherford elastic cross sections, including relativistic effects, is (Newbury & Myklebust, 1981)

$$\sigma_{el}^i = 5.21 \times 10^{-21} \left(\frac{Z_i}{E_j} \right)^2 \frac{4\pi}{\delta_i(1 + \delta_i)} \left(\frac{E_j + m_0 c^2}{E_j + 2m_0 c^2} \right) \quad (\text{cm}^2), \quad (1)$$

where σ_{el}^i is the total elastic cross section of the element i , Z_i is the atomic number of element i , E_j is the energy (in kiloelectron volts) of the incident electron at the point P_j , and $m_0 c^2$ is the electron rest energy (equal to 511 keV). The screening parameter δ_i of the element i takes into account the diminution of the net charge of the atom due to the atomic electrons. In this work, the screening parameter of Henoc and Maurice (1976) is used:

$$\delta_i = \frac{3.4 \times 10^{-3} Z_i^{2/3}}{E_j}. \quad (2)$$

Computation of the Distance between Elastic Collisions

A knowledge of the total elastic cross section allows computation of the total elastic mean free path between collisions of a compound having n elements, λ_{el} , which is given by (Kyser, 1979)

$$\frac{1}{\lambda_{el}} = \rho N_0 \sum_{i=1}^n \frac{c_i \sigma_{el}^i}{A_i}, \quad (3)$$

where c_i is the weight fraction of element i , A_i is the atomic weight of element i , N_0 is Avogadro's number, and ρ is the specimen mass density, which is computed by this equation:

$$\rho = \frac{1}{\sum_{i=1}^n \frac{c_i}{\rho_i}}, \quad (4)$$

where ρ_i is the mass density of element i . Equation (4) assumes an ideal solution for a homogeneous phase and gives a weight-averaged density of all elements in the sample. If the true density of the compound or alloy is known, it should be used instead of the value given by equation (4).

Knowing the elastic mean free path between collisions, the distance between collisions, L_j , can be computed using the relation (Reimer, 1985)

$$L_j = -\lambda_{el} \ln(R_1), \quad (5)$$

where R_1 is a random number that is uniformly distributed between 0 and 1. In *Win X-ray*, the user can choose among four random number generators (RNGs) of Press et al. (1992), the functions RAN1, RAN2, RAN3, and RAN4. The function RAN3 is chosen by default for its speed and long period, and also our experience has shown that it is not a biased random number generator when applied to this kind of Monte Carlo simulation. In computing σ_{el}^i and λ_{el} , the energy of the electron at the point P_j is used.

Computation of the Angles of Collisions

When an elastic collision occurs, the polar angle of elastic collision, θ_j , must be computed. To compute it, the partial elastic cross section of element i with respect to the solid angle Ω , $(\partial\sigma/\partial\Omega)_i$, is used in the following equation as shown by Reimer (1985):

$$R_2 = \frac{\int_0^{\theta_j} \left(\frac{\partial\sigma}{\partial\Omega} \right)_i \sin\theta d\theta}{\int_0^\pi \left(\frac{\partial\sigma}{\partial\Omega} \right)_i \sin\theta d\theta}, \quad (6)$$

where R_2 is another random number uniformly distributed between 0 and 1. When tabulated Mott cross sections are used, equation (6) has no analytical solution and tabulated values of R_2 versus θ_j must be used in order to compute the polar angle of collision. When the partial Rutherford cross section is used in equation (6), the following equation is obtained for the evaluation of θ_j :

$$\cos\theta_j = 1 - \frac{2\delta_i R_2}{1 + \delta_i - R_2}, \quad (7)$$

where δ_i is the screening parameter.

To solve equations (6) or (7) for the computation of θ_j , the atom responsible for the elastic scattering at the point P_{j+1} must be determined for a system having more than one

element. A set of n probabilities ($P_1, \dots, P_k, \dots, P_n$) is thus defined in the following way (Kyser, 1979):

$$P_k = \frac{\sum_{i=1}^k \frac{c_i \sigma_{el}^i}{A_i}}{\sum_{i=1}^n \frac{c_i \sigma_{el}^i}{A_i}}. \quad (8)$$

A random number R_3 is then generated, uniformly distributed between 0 and 1. The incident electron collides with the k th atom if

$$P_{k-1} \leq R_3 < P_k. \quad (9)$$

The azimuth angle ϕ_j is uniformly distributed between 0 and 2π when the incident electron energy is greater than 100 eV, where spin polarization effects are negligible. Because the simulations in this work are performed for energies much greater than 100 eV, ϕ_j is computed using this equation:

$$\phi_j = 2\pi R_4, \quad (10)$$

where R_4 is another random number uniformly distributed between 0 and 1.

Computation of Energy Loss

The energy of an electron moving from the point P_j to P_{j+1} is determined by the continuous slowing down approximation:

$$E_{j+1} = E_j + \frac{dE}{dS} L_j, \quad (11)$$

where dE/dS is the rate of energy loss at energy E_j . To compute dE/dS , the modification of Joy and Luo (1989) of the Bethe equation is used:

$$\frac{dE}{dS} = -7.85 \times 10^4 \frac{\rho}{E_j} \sum_{i=1}^n \frac{c_i Z_i}{A_i} \ln \left(\frac{1.166 E_j}{J_i^*} \right) \quad (\text{keV/cm}), \quad (12)$$

where J_i^* is the modification of the mean ionization potential of element i given by the following equations, as suggested by Joy and Luo (1989):

$$J_i^* = \frac{J_i}{1 + k_i \frac{J_i}{E_j}}, \quad (13a)$$

$$J_i = 11.5 Z_i \quad (\text{eV}) \quad Z_i < 13, \quad (13b)$$

and

$$J_i = 9.76 + 58.5 Z_i^{-0.19} \quad (\text{eV}) \quad Z_i \geq 13 \quad (13c)$$

and k_i is given by

$$k_i = 0.734 Z_i^{0.037}, \quad (14)$$

which was obtained by Gauvin and L'Espérance (1992) from the values published by Joy and Luo (1989). Equation (12) has been shown to be accurate to energy as low as 100 eV by Joy et al. (1995), where the classical Bethe equation fails for electron energies smaller than about six times the mean ionization energy ($E_j < 6J_j$).

Computation of X Rays

In this Monte Carlo simulation program, X rays are generated between each collision, and the $\varphi(\rho z)$ curves are computed for the characteristic lines and for the Bremsstrahlung. After the simulation of a fixed number of electron trajectories, the emitted X rays are computed by performing the integration of the $\varphi(\rho z)$ curves multiplied by the absorption correction and the intensity of the thin film used to normalized the $\varphi(\rho z)$ curves.

For each characteristic line, the $\varphi(\rho z)$ curves are computed as follows (see the Appendix for the derivation):

$$\varphi_{nl}^i(\rho z_j) = \frac{\sum_k^{N_j^*} Q_i(\bar{E}_k, E_{nl}) L_k}{N Q_i(E_0, E_{nl}) t_0}, \quad (15)$$

where $Q_i(\bar{E}_k, E_{nl})$ is the ionization cross section of element i for a specific shell (the K , L_{III} , and M_V shells are considered in this work) of ionization energy E_{nl} at an electron energy \bar{E}_k , which is described by equation (21) below, L_k is the distance traveled by the electron in the layer j of thickness t_0 , and N is the total number of electron trajectories simulated. In equation (15), the summation is performed for all the electron trajectories when they cross the specific layer j of thickness t_0 , the number of such electrons being N_j^* . The number of such layers in the simulations is a parameter of *Win X-ray* but typically, 50 to 100 layers are needed to obtain reliable results. The parameterization of Casnati et al. (1982) of the ionization cross sections is used because it is the most accurate when compared with experimental data for K lines, as shown by Gauvin (1993). Casnati et al. (1982) did not parameterize the L and M cross sections, but we have decided to use their basic equation and to adjust the parameters for these lines with experimental X-ray spectra involving L and M lines. Their equation to compute

the ionization of a specific shell, $Q_i(\bar{E}_k, E_{nl})$, from an incident electron of energy \bar{E}_k is

$$Q_i(\bar{E}_k, E_{nl}) = \frac{Z_{nl} a_0^2 C R^2 \psi \phi}{E_{nl}^2 U} \ln(U), \quad (16)$$

where Z_{nl} is the number of electrons in the nl -shell (where n and l are the quantum numbers associated with this shell), a_0 is the Bohr radius (52.9 pm), R is the Rydberg energy (13.6 eV), E_{nl} is the ionization energy of the nl -shell (in electron volts), U is the overvoltage ratio given by \bar{E}_k/E_{nl} , and ψ is given by

$$\psi = \left(\frac{E_{nl}}{R} \right)^d, \quad (17)$$

where

$$d = -0.0318 + \frac{0.3160}{U} - \frac{0.1135}{U^2}. \quad (18)$$

In equation (16), ϕ is given by

$$\phi = 10.57 \cdot \exp\left(-\frac{1.736}{U} + \frac{0.317}{U^2}\right) \quad (19)$$

and C is a relativistic correction factor (Gryzinski, 1965):

$$C = \frac{(2+I)}{(2+\tau)} \left[\frac{(1+\tau)}{(1+I)} \right]^2 \left\{ \frac{(I+\tau)(2+\tau)(1+I)^2}{\tau(2+\tau)(1+I)^2 + I(2+I)} \right\}^{3/2}, \quad (20)$$

where $I = E_{nl}/m_0 c^2$ and $\tau = \bar{E}_k/m_0 c^2$. To compute the ionization cross section using equations (16)–(20), the mean energy \bar{E}_k , defined above, is computed using this equation:

$$\bar{E}_k = \frac{E_j + E_{j+1}}{2}, \quad (21)$$

where E_j and E_{j+1} are the k electron's energy at point P_j and P_{j+1} , respectively. X rays are assumed to be generated continuously between those two points, and the corrected distance traveled in each layer, L_k , is computed. An efficient algorithm was developed for this purpose.

For the computation of the bremsstrahlung X rays, N_w energy windows are set as an input parameter and the energy of each window, E_l is given by

$$E_l = I \times \left(\frac{E_0}{N_w} \right) - \left(\frac{E_0}{2N_w} \right), \quad (22)$$

where $1 \leq l \leq N_w$ and E_0 is the initial energy of the incident electrons. For each window where $E_l < \bar{E}_k$ (the electron energy at the point P_{j+1}), the corresponding $\varphi(\rho z)$ curve for the generation of the bremsstrahlung is computed (see the Appendix for a derivation):

$$\varphi_l^B(\rho z_j) = \frac{\sum_k^{N_j^*} \left(\sum_i^n Q_i(\bar{E}_k, E_l, \theta_k) \frac{c_i}{A_i} \right) L_k}{N \left(\sum_i^n Q_i(E_0, E_l, \theta_0) \frac{c_i}{A_i} \right) t_0}, \quad (23)$$

where $Q_i(\bar{E}_k, E_l, \theta_k)$ is the cross section for bremsstrahlung generation of element i (of weight fraction c_i and atomic weight A_i) for a photon of energy E_l and for an incident electron of energy \bar{E}_k , θ_k is the angle between the line of the electron trajectory (between the points P_j and P_{j+1}) and detector's axis, and θ_0 is a reference angle. In this work, the bremsstrahlung cross sections from the theory of Kirkpatrick and Wiedmann (1945) are used (equations (24)–(37)):

$$Q_i(\bar{E}_k, E_l, \theta_k) = 8.87 \times 10^{-28}$$

$$\times \frac{Z_i^2}{k\tau} \left\{ I'_X \frac{\sin^2 \theta_k}{(1 - \beta \cos \theta_k)^4} + I'_Y \left[1 + \frac{\cos^2 \theta_k}{(1 - \beta \cos \theta_k)^4} \right] \right\} \quad (\text{cm}^2/\text{Str}), \quad (24)$$

where β is the ratio of the speed of the electron to that of the speed of light, I'_x is given by

$$I'_X = 0.252 + c_1 \left(\frac{k}{\tau} - 0.135 \right) - c_2 \left(\frac{k}{\tau} - 0.135 \right)^2, \quad (25)$$

where τ is the kinetic energy of the electron in $m_0 c^2$ units ($\tau = \bar{E}_k/m_0 c^2$) and k is the energy of the emitted photon in $m_0 c^2$ units ($k = E_l/m_0 c^2$). In equation (25), c_1 and c_2 are given by the following equations:

$$c_1 = 1.47C_2 - 0.507C_1 - 0.833 \quad (26)$$

and

$$c_2 = 1.70C_2 - 1.09C_1 - 0.627. \quad (27)$$

In equations (26) and (27), C_1 and C_2 are given by the following equations:

$$C_1 = e^{-0.223(V/Z_i^2)} - e^{-57(V/Z_i^2)} \quad (28)$$

and

$$C_2 = e^{-0.0828(V/Z_i^2)} - e^{-84.9(V/Z_i^2)}, \quad (29)$$

where

$$V = 1703\tau. \quad (30)$$

In equation (24), I'_Y is given by this equation:

$$I'_Y = -d_2 + \frac{d_3}{\left(\frac{k}{\tau} + d_1\right)}, \quad (31)$$

where

$$d_1 = \frac{-0.214D_1 + 1.21D_2 - D_3}{1.43D_1 - 2.43D_2 + D_3}, \quad (32)$$

$$d_2 = (1 + 2d_1)D_2 - 2(1 + d_1)D_3, \quad (33)$$

and

$$d_3 = (1 + d_1)(D_3 + d_2). \quad (34)$$

To compute equations (32)–(34), the following equations are needed:

$$D_1 = 0.220[1 - 0.390e^{-26.9(V/Z_i^2)}], \quad (35)$$

$$D_2 = 0.067 + \frac{0.023}{\frac{V}{Z_i^2} + 0.75}, \quad (36)$$

and

$$D_3 = -0.00259 + \frac{0.00776}{\frac{V}{Z_i^2} + 0.116}. \quad (37)$$

The emitted intensity is computed in the following manner. The value of $\varphi(\rho z_j)$, in equation (A7), is multiplied by the intensity for a thin film, equation (A6), and by the absorption probability of the X ray by the specimen (exponential term in the summation) to give the value emitted from a depth ρz_j . The overall emitted intensity obtained by summing the X rays emitted from all of the slices is multiplied by the number of electrons striking the sample, it/e , to obtain the X-ray intensity as a function of the probe current where i is in amperes, the live acquisition time t is in seconds, and e is the electron charge. This intensity is

multiplied by the detector efficiency $\varepsilon(E_{nl})$ and the fraction of the solid angle ($\Omega_D/4\pi$) to give the total number of characteristic X-ray photons detected by an EDS detector with a solid angle of Ω_D , I_{nl}^i :

$$I_{nl}^i = \left(\frac{\Omega_D}{4\pi}\right) \frac{it}{e} \varepsilon(E_{nl}) Q_i(E_0, E_{nl}) \omega_i(E_{nl}) \alpha_i(E_{nl}) \frac{c_i}{A_i} N_0 \rho t_0 \times \sum_j^{N_L} \varphi_j^i(\rho z_j) \cdot \exp\left(-\chi\left((j-1) + \frac{1}{2}\right)\Delta(\rho z)\right). \quad (38)$$

In the previous equation, N_0 is Avogadro's number. The fractional solid angle ($\Omega_D/4\pi$), assuming a point source for the generation of X rays, can be evaluated by using this equation (Tsoulfanidis, 1995):

$$\left(\frac{\Omega_D}{4\pi}\right) = \frac{1}{2} \left[1 - \frac{D}{\sqrt{D^2 + R^2}}\right], \quad (39)$$

where D is the distance between the electron beam and the detector and R is the active EDS detector radius (if a collimator is present in front of the detector, R is its radius).

In equation (38), χ is given by this equation:

$$\chi = \left(\sum_{i=1}^n c_i \frac{\mu}{\rho}\right) \operatorname{cosec} \Psi, \quad (40)$$

where $\mu/\rho|_i^l$ is the mass absorption coefficient of a photon of energy E_l in element i and Ψ is the takeoff angle of the X-ray detector, between the specimen surface and the centerline of the X-ray detector.

In equation (38), $\omega_i(E_{nl})$ is the fluorescence yield of the characteristic line, and the values tabulated by Goldstein et al. (1992) are used. The parameter $\alpha_i(E_{nl})$ is the weight of the characteristic line for a given family and the parameterization of Schreiber and Wims (1982) was used. In this work, the following characteristic lines are considered: K_{α_1} , K_{α_2} , K_{β_1} , K_{β_2} , L_{α} , L_{β_1} , L_{β_2} , L_{γ} , and M_{α} . The detector efficiency is computed using the equation given by Goldstein et al. (1992):

$$\varepsilon(E_{nl}) = e^{-(\mu/\rho)_{Au}^{Enl} \rho_{Au} t_{Au} + (\mu/\rho)_{Si}^{Enl} \rho_{Si} t_{Si}} (1 - e^{-\mu/\rho_{Si}^{Enl} \rho_{Si} x_{Si}}), \quad (41)$$

where t_{Au} is the gold layer thickness (a value of 10 nm is set as a default value), t_{Si} is the silicon dead layer (a value of 200 nm is set as a default value), and x_{Si} is the thickness of the silicon crystal (a value of 3 mm is set as a default value). In this program, one can choose among three parameterizations of the mass absorption coefficients: Heinrich (1966),

Thin and Leroux (1979), and Henke et al. (1993); by default the program uses the MAC from Henke.

The total background intensity, for each energy window, I_l^B , is computed as follows:

$$I_l^B = \left(\frac{\Omega_D}{4\pi} \right) \frac{it}{e} \varepsilon(E_X) \left(\sum_i^n Q_i(E_0, E_X, \theta_0) \cdot \frac{c_i}{A_i} \right) N_0 \rho t_0 \times \sum_j^{N_L} \varphi_l^B(\rho z_j) \cdot \exp\left(-\chi \left((j-1) + \frac{1}{2} \right) \Delta(\rho z)\right), \quad (42)$$

where θ_0 is the angle between the incident electron and the detector axis and $\varepsilon(E_l)$ is the detector efficiency of the energy window E_l , computed using equation (41). After the windows of background intensities are computed using equation (43), they are interpolated to 1024 channels using splines (Press et al., 1992).

For the characteristic lines and the bremsstrahlung, the resolution of the detector is taken into account by convolution. The resolution of a photon is given by its full width at half maximum, ΔE_{FWHM} , by this equation (Reimer, 1985):

$$\Delta E_{\text{FWHM}} = \sqrt{(\Delta E_{\text{Noise}})^2 + 2.35^2 \varepsilon_{hp} F E_p}, \quad (43)$$

where E_p is the photon energy, ε_{hp} is the mean energy needed to create an electron-hole pair (3.8 eV for Si) in the detector, F is the Fano factor of the detector (0.125 for an ideal Si detector), and ΔE_{Noise} is the electronic noise of the detector. In *Win X-ray*, ΔE_{Noise} is set by default to 50 eV. However, real EDS detectors have different resolution parameters, and the real noise contribution as well as the true Fano factor can be obtained by solving equation (43) with the measured ΔE_{FWHM} of a low and a high energy line. Assuming Gaussian peak shapes, the standard deviation σ of a characteristic line is given by the following equation:

$$\sigma = \frac{\Delta E_{\text{FWHM}}}{2.3548}. \quad (44)$$

Then, the intensity corresponding to the specific channels can be computed.

ADJUSTMENTS OF THE SIMULATED X-RAY SPECTRA

The absolute values of the detected X-ray intensities are given by equations (38) and (42), as shown in the previous section. These two equations depend on several parameters, and any error in their determination will lead to incorrect values of the predicted X-ray intensity. For example, the accuracy of the fractional solid angle of the detector is determined by the accuracy of the measurements of the

distance D and the radius R , as given in equation (39). It is difficult to measure D and R ; thus, there will be uncertainty in the fractional solid angle used. Furthermore, the transmission factor of the silicon grid used in support of most thin window EDS detectors is generally not accurately known. The probe current variation during the spectrum acquisition is another source of error. The default detector efficiency is calculated using the nominal values of the crystal properties (metallic contact layer, dead layer thickness, crystal thickness, and the vacuum windows properties, where it is assumed that there is no icing on the front window). However, any error in these parameters will have a cumulative effect on detector efficiency as calculated by equation (41). The absolute value of the detected X-ray intensity will also be affected by any inaccuracy in the models used for the X-ray generation (ionization cross sections, fluorescence yield, line fraction), electron transport (elastic cross section, energy loss), and photon transport (mass absorption coefficient). In this work, as a first approximation for all of these errors, four adjustment factors were determined using an experimental database of X-ray spectra. These factors allow the comparison of the experimental spectra with the simulated spectra. Equations (45)–(48) show how the adjustment factors (F_K , F_L , F_M , and F_B) are used in the calculation of the X-ray intensity of the spectra:

$$I_l^B(\text{eff}) = F_B I_l^B \quad (45)$$

$$I_K^i(\text{eff}) = F_K I_K^i \quad (46)$$

$$I_L^i(\text{eff}) = F_L I_L^i \quad (47)$$

$$I_M^i(\text{eff}) = F_M I_M^i, \quad (48)$$

where I_l^B , for a given photon energy, is given by equation (42) and I_K^i , I_L^i , and I_M^i are given by equation (38). The effective intensity $I_X^i(\text{eff})$ is used for comparison with the experimental results. In the initial approach, these adjustment factors were assumed to be multiplicative constants independent of atomic number and incident energy because it is the simplest approach with perhaps the exception of assuming all of the factors are the same, as would be the case if the theory were perfect, but the solid angle, for example, was off by a constant. The authors are very aware of the fact that equations (45)–(48) are a gross oversimplification, but have simply used them as a starting point for further refinement of the model.

To determine how far off this assumption is the bremsstrahlung and characteristic X-ray cross sections were adjusted using experimental spectra acquired with the NIST suite of copper/gold alloy wires (SRM 482) with Au compositions of 0%, 20%, 40%, 60%, 80%, and 100%. The wires were mounted in lead/tin solder and metallographically polished. The spectra were acquired with incident electron energies of 5, 10, 15, 20, 25, and 30 keV for 100 s (live time)

using a JEOL 840A equipped with an EDAX Phoenix EDS system. The microscope/specimen geometry was set up to provide optimum conditions for analysis: detector process time 100 μ s, takeoff angle 30°, and dead time 30% (1000 cps). For each composition and energy, three spectra were taken at different positions on the sample. The nominal values of the solid angle of the detector as well as its nominal detection efficiency were used and the specimen current was measured with a Faraday cup before and after each series of three spectra. Only spectra taken with beam current variations lower than 1% have been used for the factor calculations.

The four adjustment factors, F_K , F_L , F_M , and F_B , were optimized for all the spectra obtained from the different Au-Cu alloys and the various incident electron energies to obtain the best agreement between the experimental and simulated spectra by minimization of the difference between the two spectra using the chi-square fitting algorithm developed by Press et al. (1992). F_K was obtained with the K_α lines of Cu, F_L was obtained with the L_α lines of Cu and Au, and F_M was obtained with the M_α lines of Au. For the bremsstrahlung adjustment factor, F_B , only the portions of each spectrum without the characteristic peaks were used. Of course, these adjustment factors are only valid for this microscope and EDS system because real values of solid angle and detector efficiencies can be different from their nominal values.

RESULTS

The first task was to determine reasonable values for the adjustment factors. Figures 2–5 show the variation of these factors with the incident electron energy and the specimen concentration. These results show that in some cases the adjustment factors are dependent on the electron incident energy and the specimen composition. In Figure 2, the variation from the chosen value of the adjustment factor for the bremsstrahlung is larger at low incident electron energy. This could be explained by the bremsstrahlung cross sections model used in this work, which is known to be less accurate at low incident electron energy. Figure 3 shows the value of the K shell factor and a small variation is seen. Figure 4 shows the value of the L shell factor, where the peak intensity for the L_α lines for copper and gold were used to optimize the adjustment factor. Above 15 keV, this adjustment factor is almost constant. For pure copper, not shown, the factor has a linear variation with the electron beam energy. This behavior is not yet explained and more accurate models of ionizations cross sections might give a better result in this case. Figure 5 shows a small variation of the adjustment factor for the M shell along the incident electron energy, but a relatively large spread of values for this factor as a function of the concentration. This behavior can be explained by the lack of accurate models currently

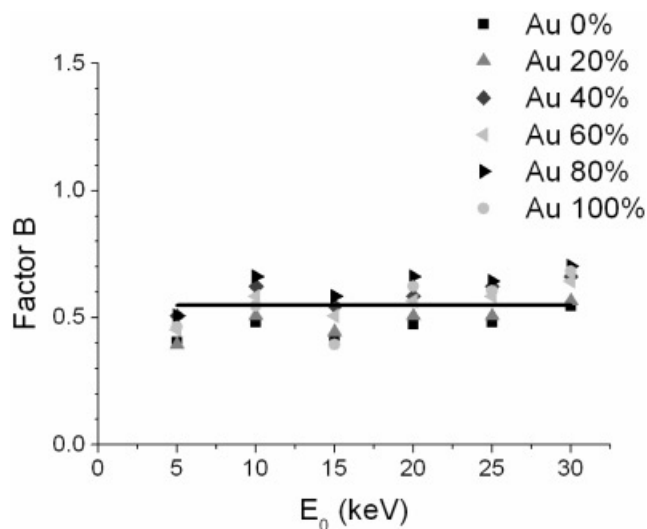


Figure 2. Adjustment factors for the bremsstrahlung calculated from an Au–Cu alloy X-ray spectra with different concentrations and incident electron energies. See the text for details.

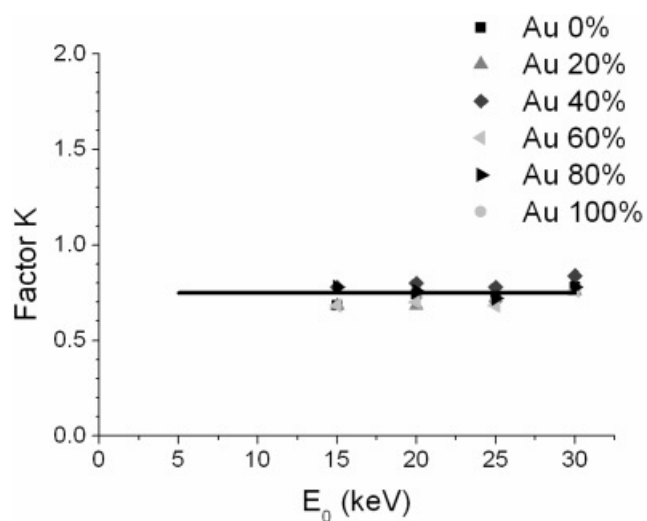


Figure 3. Adjustment factors for the K shell calculated from an Au–Cu alloy X-ray spectra with different concentrations and incident electron energies. See the text for details.

available for the computation of ionization cross sections for M shells. Because the M_β peak is not simulated and a peak overlap is observed for the M family peaks for gold, the calculation yields a greater value of the adjustment factor, as seen in Figure 6 for the spectrum labeled “best” where the value of the intensity of the M_α line has to be higher to compensate for the missing M_β line. Therefore, the value of the adjustment factor used is smaller to give correct M_α line intensity, as shown in Figure 6 for the spectrum labeled “currently used.”

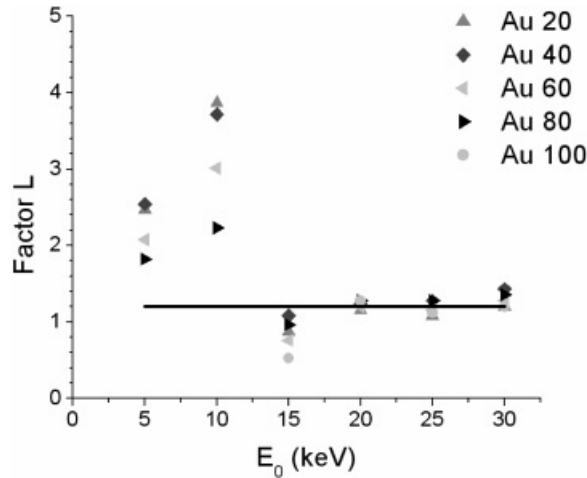


Figure 4. Adjustment factors for the L shell calculated from an Au–Cu alloy X-ray spectra with different concentrations and incident electron energies. See the text for details.

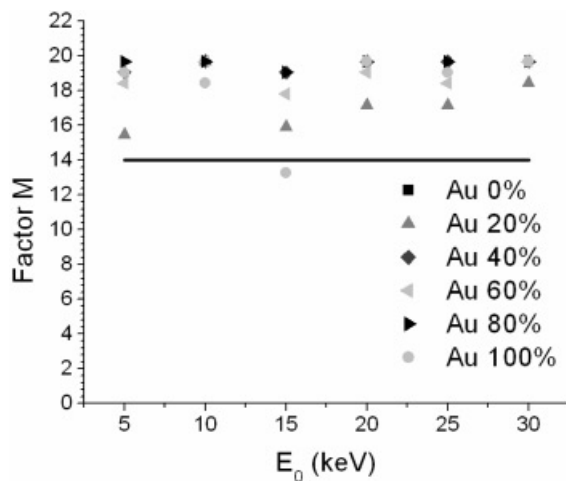


Figure 5. Adjustment factors for the M shell calculated from an Au–Cu alloy X-ray spectra with different concentrations and incident electron energies. See the text for details.

From the results presented in Figures 2–5, the mean value was calculated for each factor for all the compositions and incident electron beam energies. The adjustment factor for the bremsstrahlung cross sections is equal to 0.55 and for the characteristic X-ray cross sections equal to 0.75, 1.2, and 14 for the K , L , and M shells, respectively. These adjustment factors are partly dependent on the cross section model used for L and M lines, the detector efficiency value, and the real solid angle. The accuracy of these factors was estimated by the calculation of the mean error for each factor with the error value for all the spectra used in this study.

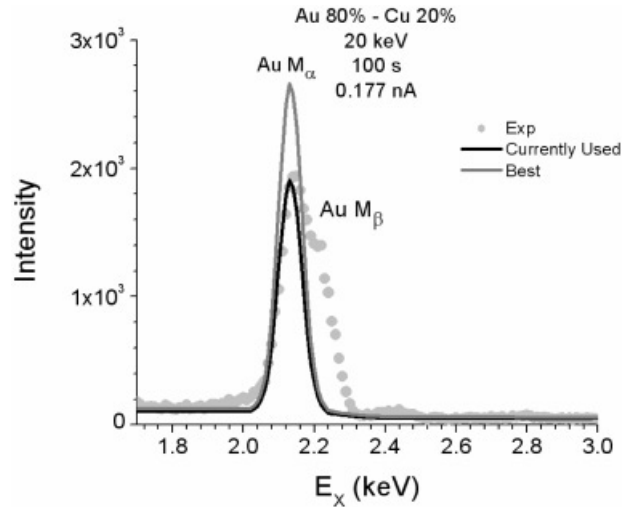


Figure 6. Comparison between a simulated and a measured (Exp) Au (80 wt%)–Cu (20 wt%) X-ray spectrum obtained at 20 keV for the gold M lines with optimized adjustment factors obtain for this particular condition (Best) and the current adjustment factors for all conditions (Currently Used).

Comparison with Computed $\varphi(\rho z)$ Curves

Figures 7 and 8 show a comparison between the $\varphi(\rho z)$ curves computed with *Win X-ray* and the PROZA program developed by Bastin et al. (1986) for the K shell of Al and Cu, respectively, at 15 keV. Some discrepancies can be observed between both models, despite a similar range of X-ray generation. A different value of $\varphi(0)$ in both models leads to differences between both models below the maximum value of the $\varphi(\rho z)$ curve. Because the PROZA model assumes $\varphi(0)$ values from a given parameterization, any errors in these values will impact the shape of the $\varphi(\rho z)$ curves. In the case of *Win X-ray*, the value of $\varphi(0)$ occurs naturally as the result of the Monte Carlo simulations. Currently, our group is performing a systematic comparison of $\varphi(\rho z)$ curves simulated with *Win X-ray*, measured experimentally and computed with several theoretical models, and these results will be published.

Effect of Incident Electron Energy on Emitted X-Ray Intensity

For practical purposes, the depth distribution of emitted rather than generated X rays is needed when absorption is significant. These curves, labeled $\psi(\rho z)$ to avoid confusion, are computed by multiplying the $\varphi(\rho z)$ curve with the exponential term correcting for absorption as follow:

$$\psi(\rho z) = \varphi(\rho z)e^{-\chi\rho z}. \quad (49)$$

Figure 9 shows the $\psi(\rho z)$ curves of emitted X rays for the K shell of pure copper simulated at 10, 15, 20, and 30 keV with

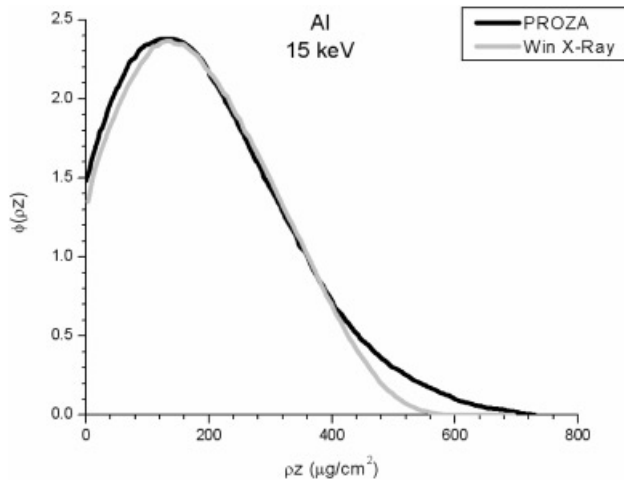


Figure 7. Comparison between the $\varphi(\rho z)$ curves computed with *Win X-ray* and the PROZA program developed by Bastin et al. (1986) for the K shell of Al at 15 keV.

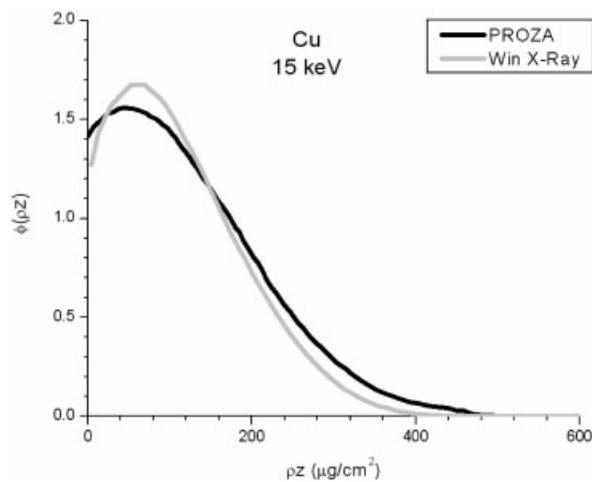


Figure 8. Comparison between the $\varphi(\rho z)$ curves computed with *Win X-ray* and the PROZA program developed by Bastin et al. (1986) for the K shell Cu at 15 keV.

10,000 electron trajectories. As expected, the maximum of the curves and its position, the value of $\psi(\rho z)$, and the range of the K -shell ionization increase with the incident electron energy, and the shapes of these curves are similar to the $\varphi(\rho z)$ curves because X-ray absorption is negligible for the K_{α} line of copper. Figure 10 shows the $\psi(\rho z)$ curves of emitted X rays for the L_{α} line of pure copper simulated at 10, 15, 20, and 30 keV. Because X-ray absorption is more significant for the L_{α} line of copper, these curves are much less sensitive to the incident electron energy than for the K_{α} line, and the variation in the depth is much smaller.

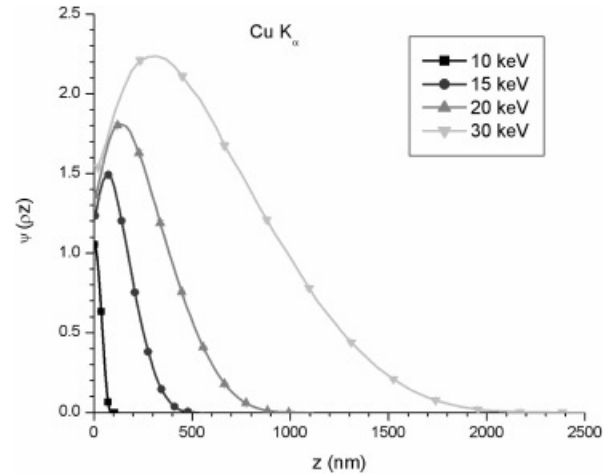


Figure 9. $\psi(\rho z)$ curves of emitted K lines X rays for pure copper simulated at 10, 15, 20, and 30 keV.

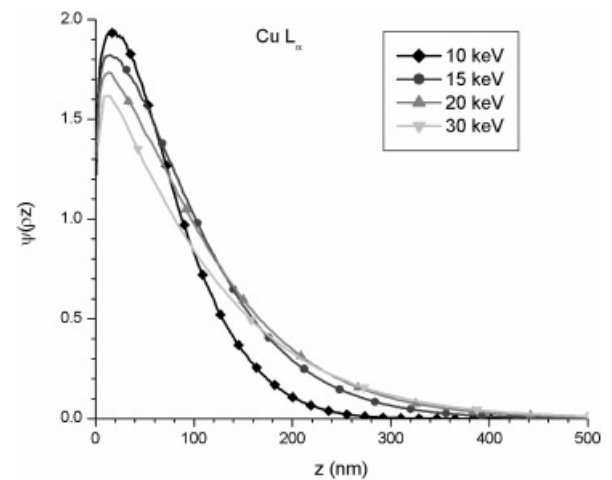


Figure 10. $\psi(\rho z)$ curves of emitted L lines X rays for pure copper simulated at 10, 15, 20, and 30 keV.

Simulation of the Bremsstrahlung of an Al-3(wt%) Mg Alloy

Because the simulation of X-ray emission is a time-consuming computer calculation, one can approximate the bremsstrahlung intensity for each EDS channel by interpolation between calculated values from a smaller number of energy windows. Figure 11 shows the effect of the number of energy windows on the bremsstrahlung spectrum for Al-3(wt%) Mg alloy at 5 keV, and Figure 12 shows the same curves simulated at 30 keV. It is clear that the shape of the bremsstrahlung curve is complex. This is caused by the increase of the mass absorption coefficient at the Al K edge that causes the strong decrease of the bremsstrahlung

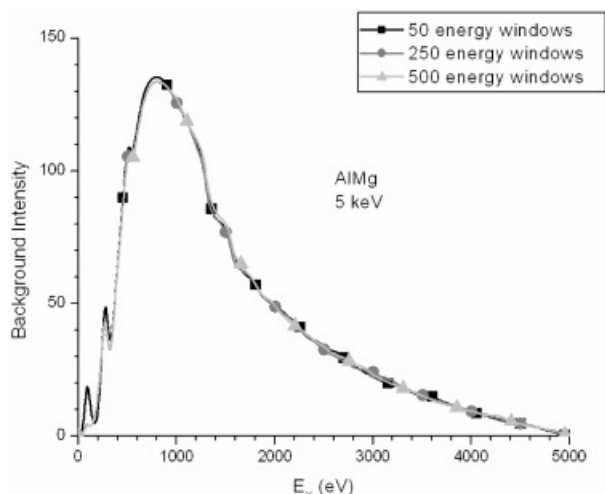


Figure 11. Simulated bremsstrahlung of an Al (97 wt%)-Mg (3 wt%) alloy at 5 keV for 50, 500, and 1024 energy windows.

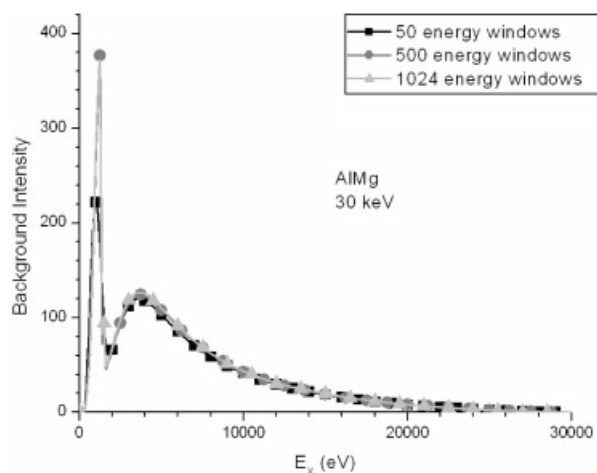


Figure 12. Simulated bremsstrahlung of an Al (97 wt%)-Mg (3 wt%) alloy at 30 keV for 50, 500, and 1024 energy windows.

intensity for photon energies greater than 1.53 keV. Figures 11 and 12 show the effect of the number of windows on the computation of the bremsstrahlung. It is obvious that 500 energy windows are as good as using 1024 windows. Even the use of 50 windows is adequate. Of course it is much faster to simulate a complete X-ray spectrum with 50 energy windows than 500, at least by a factor of 10. Figure 13 shows the ratio of the Mg K_{α} intensity estimated with linear interpolation of the bremsstrahlung (I_{LB}) to that of the true Mg K_{α} intensity (I_{True}), as a function of the number of simulated bremsstrahlung energy windows. It is clear that significant mistakes on the evaluation of the Mg K_{α} net intensity can be performed with linear interpolation and that the error increases with electron beam energy because of the increased effect of absorption on the true

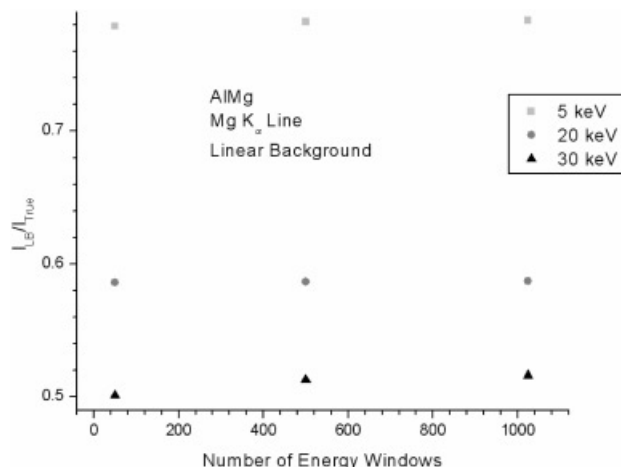


Figure 13. Ratio of the Mg K_{α} intensity estimated with linear interpolation of the bremsstrahlung (I_{LB}) to that of the true Mg K_{α} intensity (I_{True}), as a function of the number of simulated bremsstrahlung energy windows for electron energy of 5, 20, and 30 keV.

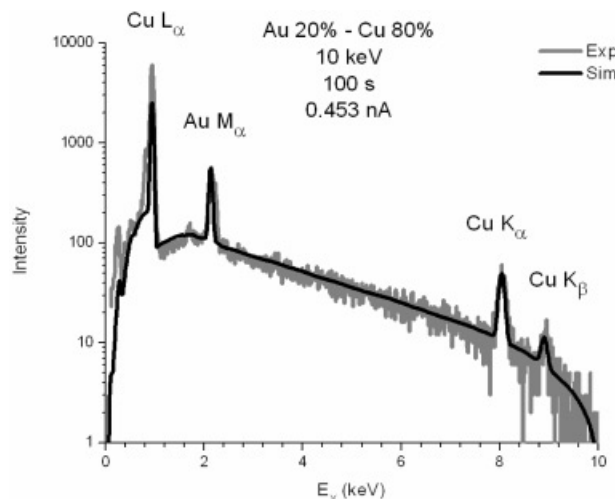


Figure 14. Comparison between a simulated (Sim) and a measured (Exp) Au (20 wt%)-Cu (80 wt%) X-ray spectrum obtained at 10 keV. See the text for details.

shape of the bremsstrahlung. The estimation of the net intensity of a characteristic line of low concentration located just above an absorption edge is a difficult task, and a Monte Carlo program, like *Win X-ray*, may be helpful.

Comparison with Experimental X-Ray Spectra

Figures 14–17 show the comparison between simulated and experimental Au–Cu alloy spectra for two concentrations (20 wt% Au and 80 wt% Au) at 10 and 30 keV. The agreement is excellent except in the two extreme regions:

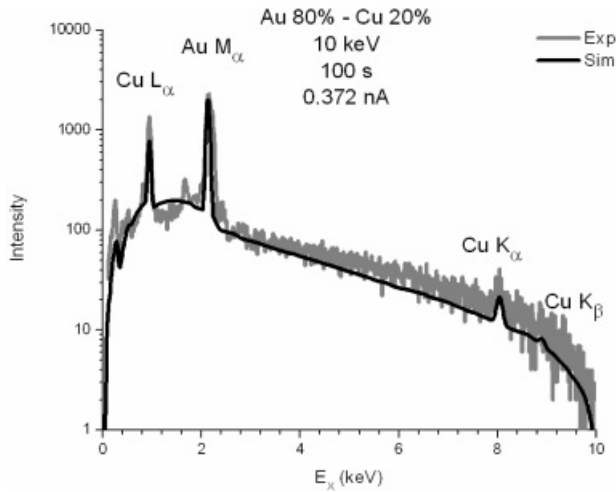


Figure 15. Comparison between a simulated (Sim) and a measured (Exp) Au (80 wt%)–Cu (20 wt%) X-ray spectrum obtained at 10 keV. See the text for details.

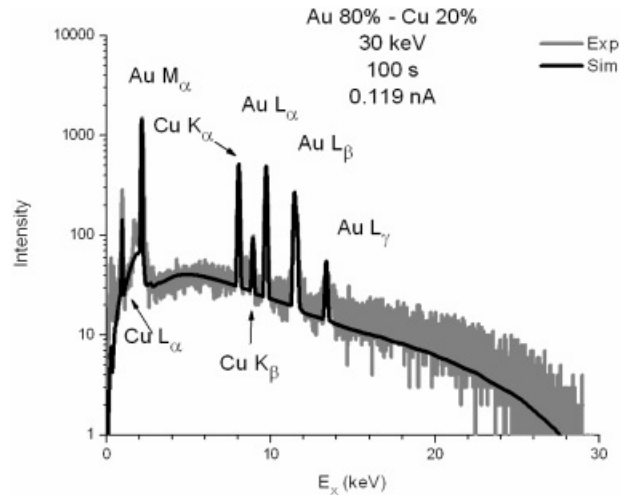


Figure 17. Comparison between a simulated (Sim) and a measured (Exp) Au (80 wt%)–Cu (20 wt%) X-ray spectrum obtained at 30 keV. See the text for details.

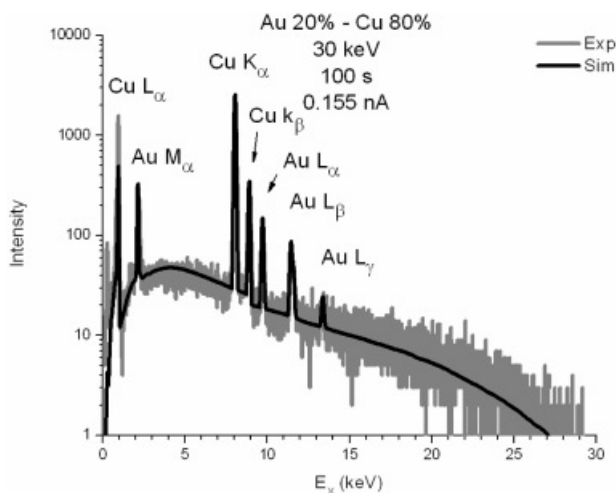


Figure 16. Comparison between a simulated (Sim) and a measured (Exp) Au (20 wt%)–Cu (80 wt%) X-ray spectrum obtained at 30 keV. See the text for details.

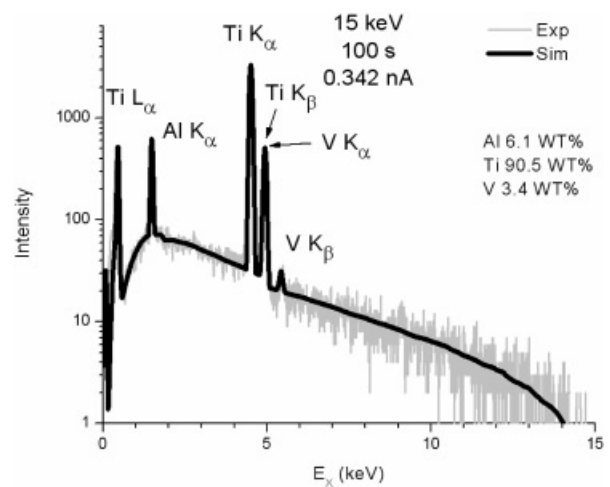


Figure 18. Comparison between a simulated (Sim) and a measured (Exp) Ti (90.5 wt%)–Al (6.1 wt%)–V (3.4 wt%) X-ray spectrum obtained at 15 keV. See the text for details.

low and high photon energy. At high photon energy the simulated bremsstrahlung is smaller than the experimental values for the Au-rich specimen because of inaccuracies in the model for the bremsstrahlung cross sections. These inaccuracies are responsible for the lower value of the simulated Duane–Hunt limit, as seen in Figures 16 and 17. At low photon energy, the disagreement is mainly due to the use of the nominal thickness for X-ray absorption in the EDS detector, giving uncertainties in the detector efficiency. Because *Win X-ray* was adjusted with the copper–gold system, the good agreement shown in Figures 14–17 is not surprising. New comparisons with elements that were not

present in the adjustment factor database are more suited to test the accuracy of *Win X-ray*.

Figure 18 shows the comparison of an X-ray spectrum measured from a Ti–Al 6.1 wt%–V 3.4 wt% alloy obtained at 15 keV and a simulated spectrum. Even though the adjustment factors were not calibrated with these elements, a good prediction is obtained using the simulation program. Figure 19 shows the comparison of an X-ray spectrum measured from an Au 20 wt%–Ag 80 wt% alloy obtained at 30 keV and a simulated spectrum. As in Figure 17, the agreement is good. However, a spectrum of the same alloy obtained at 5 keV shows a less good agreement for photons

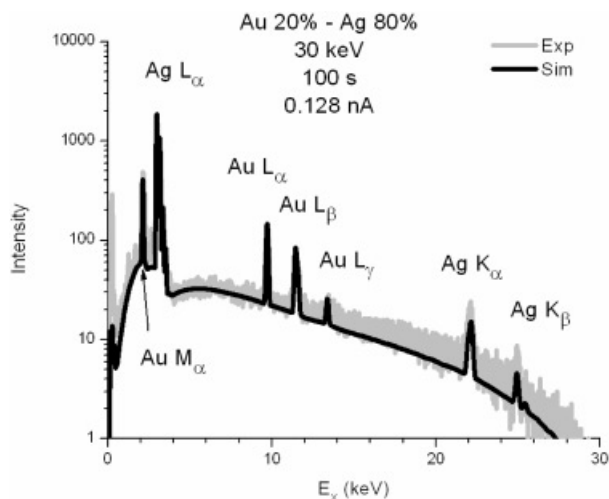


Figure 19. Comparison between a simulated (Sim) and a measured (Exp) Au (20 wt%)-Ag (80 wt%) X-ray spectrum obtained at 30 keV. See the text for details.

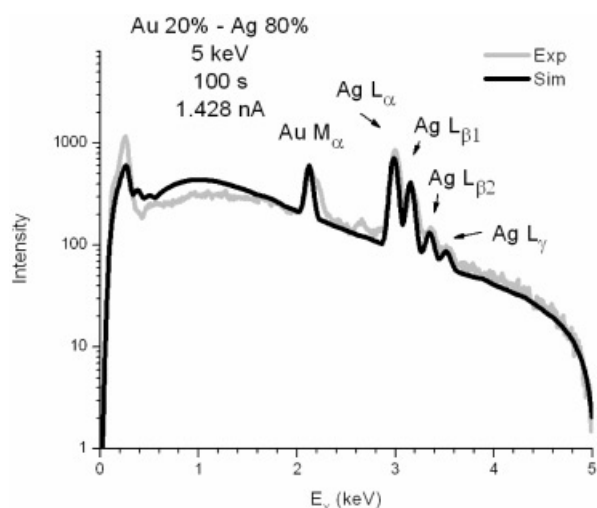


Figure 20. Comparison between a simulated (Sim) and a measured (Exp) Au (20 wt%)-Ag (80 wt%) X-ray spectrum obtained at 5 keV. See the text for details.

below 2 keV, as seen in Figure 20. This is attributed to the failure of the model of the bremsstrahlung cross sections used in this work, which tends to overestimate significantly the production of photons at photon energies 0.3 and 2 keV. This is a limitation of *Win X-ray* for the prediction of the shape of X-ray spectra for low voltage X-ray microanalysis.

DISCUSSION

In the absence of any spurious signals such as unwanted X-ray scattering in the specimen chamber, the ability to

predict complete X-ray spectra for a given sample in an SEM for a specified beam energy, beam current, electron incident angle, and X-ray takeoff angle depends on the following: the physical model used to describe X-ray generation and absorption, the solid angle of the X-ray detector, the efficiency of that detector as a function of X-ray energy, and the resolution of the detector as a function of X-ray energy. The initial choice of using only four fixed adjustment factors for the comparison of the simulated and experimental spectra has been guided by the goal to first simplify the calculation as much as possible by minimizing the number of adjustable parameters needed to ensure a good fit between experiment and theory over a broad range of materials and operating conditions. In fact, if a model correctly calculated all of the emitted X-ray intensities, only one constant would be needed to describe the spectrum entering the X-ray detector because both the characteristic line intensities of all spectral series and the background scale linearly with beam current. However, as mentioned previously, determining the solid angle of a detector, and thus the number of photons entering the detector, is difficult to do even if one is provided with engineering drawings of the detector because information may not be accurate enough or details like the window transmission through the support grid may be missing. One way to avoid this difficulty would be to have accurate experimental values of the absolute yield of a single line of an element with minimal absorption, like Cu K_{α} . This would be very helpful because the solid angle of the detector could then be easily calculated from the ratio of measured and calculated values of the line intensities. Joy (1998) has recently summarized these results and the value for Cu K_{α} is probably known to near 5% accuracy. In addition to establishing the solid angle of the detector, its efficiency must also be accurately known. Recently, Scholze and Procop (2002) have reported the measurement of detection efficiency of Si(Li) EDS detectors using synchrotron radiation. With such a calibrated detector, complete X-ray spectra could be measured with high accuracy using several specimens with mean atomic numbers ranging from boron ($Z = 5$) to gold ($Z = 79$) for various electron beam energies ranging from 3 keV to 30 keV. Finally, if the detector efficiency and solid angle are well established then the major cause for any discrepancies between theory and experiment will be in either the physical assumptions made in the Monte Carlo model or the quality of the parameters used in the calculations. As an example, there is a lack of models and measurements especially for the M lines, and the available measurements are rather sparse for the L lines. Also, an improved model of bremsstrahlung cross sections for incident electron energies smaller than 10 keV will have to be implemented. Given all of the complexities described here, even a simple four-parameter optimization of the Monte Carlo modeling has been quite successful (often better than 10% relative accuracy) in predicting complete X-ray spectra measured with an EDS on an SEM. Therefore, this work

must be viewed as a first step toward developing even more improved models with the ultimate goal of simulating accurately the absolute intensity of X-ray spectra to do true standardless analysis with better than 5% relative accuracy. This work is currently underway using a new set of reference data obtained from a broad range of elements and beam energies. Once this phase of the project is completed, then it will be easier to move toward more complex problems like the detectability of small particulates embedded in a matrix or analysis of rough surfaces. In that context, Monte Carlo simulations will be more useful than analytical models developed to compute X-ray spectra, like the work of Duncumb et al. (2001), because these simple models cannot handle X-ray emission from complex geometries.

CONCLUSIONS

A new Monte Carlo program to simulate the complete X-ray spectrum of a given material of homogeneous composition has been developed. This program is expected to give correct approximations for the *K*, *L*, and *M* lines of any element as well as a good first-order estimation of the bremsstrahlung intensity. This program is not accurate for photon energies below 2 keV when the incident electron energy is smaller than 10 keV because of a limitation in the X-ray model used.

The adjustment factors used for the comparison between the simulated and experimental spectra have shown the weakness of some of the physical models used and limitation in the knowledge of the microscope parameters, particularly for incident electron energies below 10 keV. Nevertheless, *Win X-ray* can give useful predictions of X-ray spectra. The physical model should be improved, particularly the ionization cross sections for the *L* and *M* lines and for the bremsstrahlung. The measurement of many X-ray spectra with a well-calibrated EDS detector is currently underway and should lead to refinements in the calculation that will give an even better fit between experimental and computed spectra.

In this study, the simulation program has been used to provide a better understanding of the X-ray generation and emission and the effect of the backscattered electron, absorption, and incident electron energy on the $\varphi(\rho z)$ curves. Monte Carlo simulation can give much information not easily obtainable experimentally or even possible.

Win X-ray also can be used to find optimum conditions to perform quantitative X-ray microanalysis in the SEM as well as to find minimum mass detection, as shown by Lifshin et al. (1998). Work to improve the quantitative prediction of simulated X-ray spectra with *Win X-ray* is currently underway in our group as well as versions of *Win X-ray* for the case of layered structures (horizontal or vertical planes) and the case of rough surfaces.

REFERENCES

- BASTIN, G.F., VAN LOO, F.J.J. & HEIJLIGERS, H.J.M. (1986). Evaluation of the use of Gaussian $\varphi(\rho z)$ curves in quantitative electron probe microanalysis: A new optimization. *X-Ray Spectrom* **13**, 91–97.
- BISHOP, H.E. (1965). Calculation of electron penetration and X-ray production in a solid target. In Proceedings of the 4th ICXOM Paris, Castaing, R., Deschamps, P. & Philibert, J. (Eds.), pp. 112–117.
- CASNATI, E., TARTARI, A. & BARALDI, C. (1982). An empirical approach to K-shell ionization cross section by electron. *J Phys B* **15**, 155–167.
- CZYZEWSKI, Z., MACCALLUM, D.O., ROMIG, A.D. & JOY, D.C. (1990). Calculations of Mott scattering cross sections. *J Appl Phys* **68**, 3066–3072.
- DING, Z.-J., SHIMIZU, R. & OBORI, K. (1994). Monte Carlo simulation of X-ray spectra in electron probe microanalysis: Comparison of continuum with experiment. *J Appl Phys* **76**, 7180–7187.
- DROUIN, D., HOVINGTON, P. & GAUVIN, R. (1997). Casino: A new era of Monte Carlo code in C language for electron beam interaction, Part II: Tabulated values of Mott cross sections. *Scanning* **19**, 20–28.
- DUNCUMB, P., BARKSHIRE, I.R. & STATHAM, P.J. (2001). Improved X-ray spectrum simulation for electron probe microanalysis. *Microsc Microanal* **7**, 341–355.
- FIORI, C.E. & SWYT, C.R. (1989). The use of theoretically generated spectra to estimate detectability limits and concentration variance in energy-dispersive X-ray microanalysis. In *Microbeam Analysis*, Russell, P.E. (Ed.), pp. 236–238. San Francisco: San Francisco Press.
- GAUVIN, R. (1993). A parameterization of K-shell ionization cross-section by electron with an empirical modified Bethe's formula. *Microbeam Anal* **2**, 253–258.
- GAUVIN, R., HOVINGTON, P. & DROUIN, D. (1995). Quantification of spherical inclusions in the scanning electron microscope using Monte Carlo simulations. *Scanning* **17**, 202–219.
- GAUVIN, R. & L'ESPÉRANCE, G. (1992). A Monte Carlo code to simulate the effect of fast secondary electrons on K factors and spatial resolution in the TEM. *J Microsc* **168** (pt. 2), 153–167.
- GOLDSTEIN, J.I., NEWBURY, D.E., ECHLIN, P., JOY, D.C., ROMIG, A.D., LYMAN, C.E., FIORI, C.E. & LIFSHIN, E. (1992). *Scanning Electron Microscopy and X-ray Microanalysis*. New York: Plenum Press.
- GRYZINSKI, M. (1965). Classical theory of atomic collision I: The theory of inelastic collisions. *Phys Rev A* **138**, 336–358.
- HEINRICH, K.F.J. (1966). X-ray absorption uncertainty. In *The Electron Microprobe*, McKinley, T.D., Heinrich, K.F.J. & Whittrey, D.B. (Eds.), pp. 296–340. New York: Wiley.
- HENKE, B.L., GULLIKWA, E.M. & DAVIES, J.C. (1993). X-ray interactions: Photoabsorption, scattering, transmission and reflection at $E = 50\text{--}30,000$ eV, $Z = 1\text{--}92$. *Atom Data Nucl Tables* **54**, 181–342.
- HENOC, J. & MAURICE, F. (1976). Characteristics of a Monte Carlo program for microanalysis study of energy loss. In *Use of Monte Carlo Calculations in Electron Probe Microanalysis and Scanning Electron Microscopy*, Heinrich, K.J., Newbury, D.E. & Yakowitz, H. (Eds.), pp. 61–95. Washington, DC: National Bureau of Standards.

- HOVINGTON, P., DROUIN, D. & GAUVIN, R. (1997). Casino: A new era of Monte Carlo code in C language for electron beam interaction, Part I: Description of the program. *Scanning* **19**, 1–14.
- JOY, D.C. (1995). *Monte Carlo Modeling for Electron Microscopy and Microanalysis*. New York, London: Oxford University Press.
- JOY, D.C. (1998). The efficiency of X-ray production at low energies. *J Microsc* **191**(pt. 1), 74–82.
- JOY, D.C. & LUO, S. (1989). An empirical stopping power relationship for low-energy electrons. *Scanning* **11**, 176–180.
- JOY, D.C., LUO, S., GAUVIN, R., HOVINGTON, P. & EVANS, N. (1995). Experimental measurements on electron stopping power. *Scan Microsc* **16**, 209–220.
- KARDUCK, P. & REHBACH, W. (1991). The use of tracer experiments and Monte Carlo calculations in the $\varphi(\rho z)$ determination for electron probe microanalysis. In *Electron Probe Quantitation*, Heinrich, K.F.J. & Newbury, D.E. (Eds.), pp. 191–217. New York: Plenum Press.
- KIRKPATRICK, P. & WIEDMANN, L. (1945). Theoretical continuous X-ray energy and polarization. *Phys Rev* **67**, 321–339.
- KYSER, D. (1979). Monte Carlo simulation in analytical electron microscopy. In *Introduction to Analytical Electron Microscopy*, Hren, J.J., Goldstein, J.I. & Joy, D.C. (Eds.), pp. 270–284. New York: Plenum Press.
- LIFSHIN, E., DOGANAKSOV, N., SIROIS, J. & GAUVIN, R. (1998). Statistical consideration in EDS. *Microsc Microanal* **4**, 598–604.
- LLOVET, X., SALVAT, F. & FERNANDEZ-VAREA, J.M. (2004). Monte Carlo simulation of electron transport and X-ray generation. II. Radiative processes and examples in electron probe microanalysis. *Microchim Acta* **145**, 111–120.
- NEWBURY, D.E. & MYKLEBUST, R.L. (1981). *A Monte Carlo Electron Trajectory Simulation for Analytical Electron Microscopy*, Geiss, R.H. (Ed.), pp. 91–98. San Francisco: San Francisco Press Inc.
- PRESS, W.H., FLANERY, B.P., TECKOLSKY, S.A. & VETTERLING, W.T. (1992). *Numerical Recipes*. Cambridge: Cambridge University Press.
- REIMER, L. (1985). *Scanning Electron Microscopy; Physics of Image Formation and Microanalysis*. Berlin: Springer-Verlag.
- SCHOLZE, F. & PROCOP, M. (2002). Measurement of detection efficiency and response functions for a Si (Li) X-ray spectrometer in the range 0.1–5 keV. *X-Ray Spectrom* **30**, 69–76.
- SCHREIBER, T.P. & WIMS, A.M. (1982). Relative intensities of K and L shell X-ray lines. In *Microbeam Analysis*, Heinrich, K.F.J. (Ed.), pp. 161–166. San Francisco: San Francisco Press Inc.
- THINH, T.P. & LEROUX, J. (1979). New basic empirical expression for computing tables of X-ray mass attenuation coefficients. *X-Ray Spectrom* **8**, 85–91.
- TSOULFANIDIS, N. (1995). *Measurement and Detection of Radiation*. New York: Hemisphere Publishing Corporation.
- VIGNES, A. & DEZ, G. (1968). Distribution in depth of the primary X-ray emission in anticathodes of titanium and lead. *Brit J Appl Phys (J Phys D)* **2**, 1309–1322.

APPENDIX

The $\varphi(\rho z)$ curve of an X-ray shell of a specific element is defined as the ratio of the generated intensity $dI(\rho z)$ of a

film of thickness $d\rho z$ located at the mass-depth ρz in a bulk specimen to that of the generated intensity $I_0^* d\rho z$ in a thin unsupported film in free space having the same thickness

$$\varphi(\rho z) = \frac{dI(\rho z)}{I_0^* d\rho z}. \quad (\text{A1})$$

Generally, the thin film is a pure element identical to that of the bulk material. Also, the thickness of the film must be small enough to avoid X-ray absorption and electron beam broadening. In this work, the thin film has the same composition as that of the layer in the bulk specimen. The $\varphi(\rho z)$ curve gives the normalized distribution of generated intensity as a function of the depth of the specimen. Because an electron beam will generate $dI = \varphi(\rho z)I_0^* d(\rho z)$ X-ray photons in a layer of thickness $d(\rho z)$, the integration of dI gives the total generated X-ray intensity for a thick sample, I_G , thus:

$$I_G = I_0^* \int_0^\infty \varphi(\rho z) d(\rho z). \quad (\text{A2})$$

If X-ray absorption inside the bulk specimen is taken into account, the emitted X-ray intensity, I_E , is given by this equation:

$$I_E = I_0^* \int_0^\infty \varphi(\rho z) e^{-\chi\rho z} d(\rho z). \quad (\text{A3})$$

Characteristic X-Rays

As the electron travels through the specimen, it will produce nl -shell ionizations for the element i until its energy \bar{E}_k falls below the value E_{nl} . The number of direct ionizations per unit path length along the electron trajectory s is given by (Vignes & Dez, 1968):

$$dn_{nl}^i = Q_i(\bar{E}_k, E_{nl}) N_0 \frac{\rho c_i}{A_i} ds, \quad (\text{A4})$$

where $Q_i(\bar{E}_k, E_{nl})$ is the ionization cross section of the nl -shell, ρ is the specimen mass density, c_i the weight fraction, N_0 is Avogadro's number, and A_i is the atomic weight of the element i . We suppose that the electron of energy \bar{E}_k is a constant (the mean electron energy between two collisions) and equation (A4) is used to calculate the number of ionizations along the path length L_k . The generated intensity $I_{nl}^i(\rho z)$ by an electron beam (of N electrons) at mass-depth ρz is given by

$$I_{nl}^i(\rho z) = \sum_k^{N^*} (Q_i(\bar{E}_k, E_{nl}) \cdot L_k) \cdot N_0 \frac{\rho c_i}{A_i} \varpi_i(E_{nl}) \alpha_i(E_{nl}), \quad (\text{A5})$$

where N^* is the number of trajectory segments produced by one primary electron at the mass-depth ρz . An event can generate an X-ray with a probability given by the ionization cross section $Q_i(\bar{E}_k, E_{nl})$ for a electron of energy \bar{E}_k multiplied by the fluorescence yield $\varpi_i(E_{nl})$ and the relative transition probability $\alpha_i(E_{nl})$.

The X-ray intensity generated in a thin film of thickness t_0 by N electron at normal incidence and with an energy equal to the incident energy E_0 (no energy loss for the electron in the thin film) is

$$I_{nl}^i(\rho t_0) = N Q_i(E_0, E_{nl}) \cdot t_0 \cdot \frac{\rho c_i N_0}{A_i} \varpi_i(E_{nl}) \alpha_i(E_{nl}). \quad (\text{A6})$$

In this case, each trajectory segment k has the same intensity and N^* it is equal to N .

The depth distribution of the ionization density $\varphi(\rho z)$ can be easily obtained with equations (A5) and (A6) to give

$$\varphi_{nl}^i(\rho z_j) = \frac{\left\langle \sum_k^{N_j^*} Q_i(\bar{E}_k, E_{nl}) L_k \right\rangle}{Q_i(E_0, E_{nl}) t_0}, \quad (\text{A7})$$

where the average of the summation of the numerator of equation (A7) is taken for N electron trajectories. The total emitted intensity can be calculated from equation (A7) by doing the summation over all mass-depth layer j (N_L is the total number of layer) and multiply $\varphi(\rho z)$ by the absorption probability $\exp(-\chi((j-1) + \frac{1}{2})\Delta(\rho z))$ and intensity I_0 of the thin film of thickness t_0 where $\Delta(\rho z)$ is the thickness of a mass-depth layer

$$I_{nl}^i = N Q_i(E_0, E_{nl}) \varpi_i(E_{nl}) \alpha_i(E_{nl}) \frac{c_i N_0}{A_i} \rho t_0 \sum_j^{N_L} \varphi_{nl}^i(\rho z_j) \cdot \exp\left(-\chi\left((j-1) + \frac{1}{2}\right)\Delta(\rho z)\right); \quad (\text{A8})$$

see equation (40) for the description of the absorption factor χ .

Bremsstrahlung X-Ray

The depth distribution of the ionization density $\varphi(\rho z)$ for the bremsstrahlung has the same form as equation (A7), but now the cross section depends on the angle between the segment of the electron trajectory and the direction to the detector (because the bremsstrahlung X-ray emission is not isotropic) at the layer j . Also a summation over all elements present in the specimen is needed to obtain the $\varphi(\rho z)$ curve for a bremsstrahlung X-ray of energy E_l

$$\varphi_l^B(\rho z_j) = \frac{\sum_k^{N_j^*} \left(\sum_i^n Q_i(\bar{E}_k, E_l, \theta_k) \cdot \frac{c_i}{A_i} \right) \cdot L_k}{N \left(\sum_i^n Q_i(E_0, E_l, \theta_0) \cdot \frac{c_i}{A_i} \right) \cdot t_0}. \quad (\text{A9})$$

The total emitted intensity for the bremsstrahlung is given by

$$I_l^B = N \left(\sum_i^n Q_i(E_0, E_l, \theta_0) \cdot \frac{c_i}{A_i} \right) N_0 \rho t_0 \sum_j^{N_L} \varphi_l^B(\rho z_j) \cdot \exp\left(-\chi\left((j-1) + \frac{1}{2}\right)\Delta(\rho z)\right). \quad (\text{A10})$$

This equation is similar to equation (A8) for the characteristic X ray but with the modification to the cross section and the summation over all elements.